RSC Advances

PAPER

View Article Online
View Journal | View Issue

Cite this: *RSC Adv.*, 2017, **7**, 3125

Highly interdigitated and porous architected ternary composite of SnS_2, g-C_3N_4, and reduced graphene oxide (rGO) as high performance lithium ion battery anodes†

Md. Selim Arif Sher Shah,[a] A. Reum Park,[a] Ali Rauf,[a] Sung Hwan Hong,[a] Youngjin Choi,[a] Juhyun Park,[c] Jaeyun Kim,[a] Woo-Jae Kim[d] and Pil J. Yoo*[ab]

SnS_2 is a two-dimensional (2D) layered transition metal dichalcogenide that has been extensively investigated as an anode for lithium ion batteries (LIBs). However, it generally undergoes a large volume change during cycling, resulting in severe capacity loss. Composites of SnS_2 with carbon-based nanomaterials could deliver improved cyclic stability and rate performance. However, there is considerable room for performance improvement. In the present work, highly interdigitated porous nano-architectures of ternary composites consisting of 2D nanomaterials of SnS_2, reduced graphene oxide (rGO), and graphitic carbon nitride (g-C_3N_4) were synthesized *via* a simple one-pot hydrothermal route. The synthesized ternary nanocomposites were characterized with high surface area, porous structure, and high pore volume. Due to the intimate face-to-face interactions offered by the 2D structured constituents, the obtained nanocomposites showed remarkably improved performances as anodes in LIBs. In particular, the galvanostatic charge–discharge performance depends on the amount of g-C_3N_4 in the nanocomposites. The composite containing 6.6 wt% g-C_3N_4 showed the best performance, attaining a specific capacity of 1248.4 mA h g^{-1} after 276 cycles with a coulombic efficiency of 99.9% at 100 mA g^{-1} along with an excellent rate performance. The outstanding performances of the composite anodes were attributed to the unique 3D porous structure, low charge transfer resistance, and high lithium ion diffusion coefficient, afforded by the synergistic effect of concurrent encompassing of rGO and g-C_3N_4 around the SnS_2 platelets.

Received 26th October 2016
Accepted 25th November 2016

DOI: 10.1039/c6ra25886g

www.rsc.org/advances

Introduction

SnS_2 is a well-studied anode material in lithium ion batteries (LIBs).[1–4] SnS_2 has been considered as a potential substitute for the graphite anode to increase specific capacity.[5–7] It has a layered CdI_2-type structure where Sn atoms are sandwiched between two layers of hexagonally close-packed sulfur atoms that are weakly bound *via* van der Waals interactions.[8–10] Such a crystallographic structure is likely to be suitable for the accessibility of lithium ions and tolerant for the compensation of the alloying/de-alloying process involving volume change in the electrodes.[11] Nevertheless, severe capacity fading of SnS_2 electrodes generally occurs due to low electrical conductivity ($<10^{-2}$ S cm^{-1}), large volume change (≥200%) during electrochemical cycling together with aggregation of SnS_2, and *in situ* formation of the alloy phase (Li_xSn, $0 \leq x \leq 4.4$).[7,12]

Among several approaches to resolve these issues, formulating composites with carbon-based materials, especially graphene, has been fruitful. On one hand, excellent conductivity of graphene increases the conductivity of the composites and improves the anode performance.[13–15] On the other hand, its flexibility greatly alleviates volume changes during cycling. As a result, such composites have shown significantly improved capacity and stability characteristics. For example, Mei *et al.* reported the composite of ultra-small SnS_2 nanocrystals decorated on a flexible surface of reduced graphene oxide (rGO) *via* refluxing at a low temperature. The obtained SnS_2/rGO nanocomposites showed a specific capacity of 1034 mA h g^{-1} after 200 cycles at 64.5 mA g^{-1}.[1] Chang *et al.* demonstrated a few layers of SnS_2/graphene hybrid synthesized through facile L-cysteine-assisted solution chemistry. The resultant hybrid structure exhibited a high specific capacity of 920 mA h g^{-1} after

[a]*School of Chemical Engineering, Sungkyunkwan University (SKKU), Suwon 16419, Republic of Korea. E-mail: pjyoo@skku.edu*

[b]*SKKU Advanced Institute of Nanotechnology (SAINT), Sungkyunkwan University (SKKU), Suwon 16419, Republic of Korea*

[c]*School of Chemical Engineering and Materials Science, Chung-Ang University, Seoul 06974, Republic of Korea*

[d]*Department of Chemical and Environmental Engineering, Gachon University, Songnam 13120, Republic of Korea*

† Electronic supplementary information (ESI) available. See DOI: 10.1039/c6ra25886g

50 cycles at a current density of 100 mA g^{-1}.[16] Recently, Gao *et al.* reported a nanocomposite system consisting of SnS_2 nanoplates attached to rGO nanoribbons *via* a chemical vapor deposition method, from which a specific capacity of 1100 mA h g^{-1} after 110 cycles at 100 mA g^{-1} was reported.[17] However, all of these capacity values do not equal the maximum theoretical capacity of SnS_2 of 1232.2 mA h g^{-1}. Therefore, there is substantial room for improvement of the SnS_2-based anode to attain its theoretical capacity.

After the discovery by Wang *et al.*, graphitic carbon nitride, g-C_3N_4 (hereafter namely CN), has drawn considerable attention due to its unique electronic and optical properties.[18] CN also has a two-dimensional (2D) layered structure in which π-conjugated graphitic planes are constructed by alternate arrangements of sp^2 hybridized carbon and nitrogen atoms.[19–21] However, CN usually suffers from low electrical conductivity because of its intrinsic porous microstructure.[22] Nevertheless, CN could be a potential candidate that is capable of replacing most carbon materials. In particular, thanks to the presence of π-electrons and a lone pair of electrons on the nitrogen atom, CN exhibits electron-rich and Lewis-base properties. At the same time, due to the presence of nitrogen (along with a small amount of hydrogen as an impurity), CN can form hydrogen bonding with other appropriate species. Therefore, at this point, it is expected to be beneficial to combine SnS_2, rGO, and CN into a single hybrid material for harnessing their mutual 2D–2D molecular interactions; this ternary nanocomposite would show unique synergistic properties, such as high capacity, excellent conductivity, high surface area, and porous microstructures.[23,24] Specifically, 2D–2D hybridization between rGO and CN would impart a much larger interfacial area and greater charge mobility than those for other types of interfacial hybridization, such as using a pair of 0D–2D (*e.g.*, nanoparticles–nanosheets) or 1D–2D (*e.g.*, nanowires–nanosheets).[24] However, realizing such 2D–2D interacting nanostructures is not trivial (especially with metal dichalcogenides or selenides), and they have been rarely reported.

In this work, we present an innovative means to construct 2D–2D interacting multilayered nanostructures *via* a facile one-pot hydrothermal synthesis, whereby the hybridization of SnS_2 with rGO and layered CN nanosheets occurs. Thiourea is employed as a source for hydrogen sulfide which converts Sn^{4+} ions into SnS_2. As mentioned, CN was chosen due to its properties of a porous structure, moderate capacity, and lattice matching 2D structures with rGO, which could increase the overall conductivity of hybrid materials while simultaneously providing a buffering effect to relieve problematic volume changes. As a result, one can create a hydrogel with a 3D interdigitated porous nano-architecture of the ternary composite of SnS_2/rGO/g-C_3N_4. Benefiting from the unique 2D–2D interacting multilayered nanostructures, in which intimate face-to-face interfacial contacts exist between two consecutively stacked components, the obtained hybrid materials could exhibit superior electrochemical properties in terms of specific capacity, cycling stability, and rate performance. The materials rendered a capacity value of 1248.4 mA h g^{-1}, which very slightly exceeds the theoretical capacity of SnS_2, along with a coulombic efficiency of ~99.9% after 276 cycles at 100 mA g^{-1}. Apart from this confirmed electrochemical performance, uniquely developed 3D architectures with mesoporous structures and high surface area can promote ternary nanocomposites to achieve excellent cyclic stability as well.

Materials and methods

Graphite powder (<20 μm, synthetic), $SnCl_4 \cdot 5H_2O$, urea and thiourea were purchased from Sigma-Aldrich. $NaNO_3$ (99.0%) was obtained from Yakuri Pure Chemicals Co. Ltd., Japan. H_2SO_4 (95.0%), $KMnO_4$ (99.3%), H_2O_2 (34.5%), $BaSO_4$, and HCl were procured from Samchun Chemical Co. Ltd., Korea. All chemicals were used as received. In all experiments, deionized (DI) water with a resistance of 18.2 MΩ was used.

Synthesis of graphene oxide (GO)

GO was synthesized following a modified Hummers method described elsewhere.[25–27] Typically, 1.0 g graphite powder and 1.0 g $NaNO_3$ were added to a beaker containing 23.0 ml of ice-cooled, concentrated H_2SO_4. 2.5 g $KMnO_4$ was slowly added to the mixture while maintaining a temperature of <5 °C. The beaker was then heated at 35 °C for 30 min, after which 46 ml of deionized (DI) water was slowly added and the temperature was increased to 98 °C. After 15 min, 140 ml of DI water was added. The synthesis was terminated with the slow addition of 10 ml of 30% H_2O_2. The obtained product was then washed with a 1 M HCl solution to remove any trace of SO_4^{2-} ions. Finally, Cl^- ions were removed by washing with DI water. The product was then dispersed in DI water and homogenized with ultrasonication for 1 h. A dispersion of GO nanosheets was made after centrifugation at 10 400*g* for 8 min.

Synthesis of graphitic carbon nitride, g-C_3N_4 (CN)

CN was synthesized according to a reported method with some modification.[28] In a typical experiment, 11 g of dried urea was heated to 550 °C at a ramp rate of 5 °C min^{-1} and maintained for 3 h. The obtained light yellow product was used as produced.

Synthesis of highly interdigitated and porous ternary composite architectures of reduced graphene oxide, SnS_2, and CN (GSC)

Typically, 15 ml of GO (~2 mg ml^{-1}) and 12 mg of CN in 5 ml water were exfoliated separately *via* ultra-sonication. 386 mg (1.1 mmol) of $SnCl_4 \cdot 5H_2O$ was added to the GO suspension and continuously stirred for 1.5 h followed by the addition of the suspension of CN. The resulting mixture was stirred for 1.5 h followed by the addition of 175 mg (~2.3 mmol) thiourea. The pH of the reaction mixture was 0.8 at room temperature. After 15 min of stirring, the resulting mixture was transferred to a Teflon-lined stainless steel autoclave. The autoclave was placed in an oven preheated at 180 °C. After 12 h, the autoclave was removed from the oven and cooled naturally. The resulting 3D hydrogel of the ternary composite was then rinsed with copious amounts of DI water to remove Cl^- ions. The hydrogel was then freeze-dried for 18 h. Composites with varying

amounts of CN were synthesized with the same method using different amounts of CN. Additionally, SnS_2, GS (rGO/SnS_2), and SC (SnS_2/CN) were synthesized in a similar way using the starting material(s) as required. In this work, the effect of CN on cyclic performance was investigated, thus ternary nanocomposites with the same amount of rGO and SnS_2, but varied amounts of CN, were synthesized following the same procedure mentioned above. Nanocomposites with 2.0%, 6.6%, and 10.5% CN were synthesized and are denoted respectively as GSC2, GSC6, and GSC10.

Characterization

Powder X-ray diffraction (XRD) patterns were obtained (D8 Focus, Bruker instrument, Germany) with Cu Kα radiation (λ = 1.5406 Å) in the 2θ range from 2° to 80° with a step size of 0.02° s^{-1}. The accelerating voltage and applied current were 40 kV and 40 mA, respectively. Scanning electron microscopy images were collected using a field-emission scanning electron microscope (FESEM, JSM-7600F JEOL, Japan). Transmission electron microscopy (TEM, JEM-3010, JEOL, Japan) was performed with an acceleration voltage of 300 kV. Raman spectra were taken using a micro-Raman spectrometer system (ALPHA 300M, WITec, Germany). The sample was loaded on a silicon wafer and focused using a 50× objective. The Brunauer–Emmett–Teller (BET) specific surface area and porosity of the samples were evaluated on the basis of nitrogen adsorption isotherms measured at −196 °C using a gas adsorption apparatus (ASAP 2020, Micromeritics, USA). All the samples were degassed at 120 °C before nitrogen adsorption measurements. The BET surface area was determined using adsorption data in the relative pressure (p/p_0) range of 0.06 to 0.2. X-ray photoemission spectroscopy (XPS) characterization was performed (ESCA 2000 instrument, VG Microtech, United Kingdom) with an Al Kα X-ray source. All binding energy values were corrected by calibrating the C 1s peak at 284.6 eV. High-resolution peaks were deconvoluted using Gaussian–Lorentzian functions with identical full width at half maxima (fwhm) values after Shirley background subtraction. TGA was performed under air at a ramp speed of 10 °C min^{-1} (Seiko Exstar 6000 (TG/DTA6100)).

Electrode preparation

A slurry was prepared by mixing 80 wt% active material with 10 wt% acetylene black and 10 wt% polyvinylidene fluoride (PVdF, Sigma-Aldrich) with a few drops of *N*-methyl pyrrolidone (Sigma-Aldrich). The resultant slurry was then coated on a copper foil and dried at 60 °C for 10 h in a vacuum oven. CR2032 type coin cells were assembled inside an argon-filled glove box (O_2 and H_2O concentration ≤0.5 ppm) using metallic lithium foil as a counter/reference electrode and Celgard separators. The electrolyte was 1.0 M $LiPF_6$ dissolved in a mixture of ethylene carbonate (EC) and diethyl carbonate (DEC) (1 : 1, v/v). The average loading of active material in each electrode was approximately 1.12 mg cm^{-2}. The galvanostatic discharge/charge cycling tests were performed at a constant current density of 100 mA g^{-1} between 0.005 V and 2.5 V on a battery test station (WBCS3000, WonATech Corp., Korea). The electronic conductivity of the electrodes was evaluated in the frequency range between 20 mHz and 1 MHz using electrochemical impedance spectroscopy (EIS, CHI6143E, CH Instruments, Inc., USA).

Results and discussion

Synthesis of the ternary nanocomposites is demonstrated in Scheme 1. First, Sn^{4+} ions are anchored on the negatively-charged GO (due to the presence of hydroxyl, carboxylate, *etc.* groups) *via* electrostatic attraction. This process enables the effective incorporation of Sn^{4+} moieties within the GO layers. At the same time, electron rich (on account of π electrons and a lone pair of electrons) CN species would interact with the positively-charged Sn^{4+} ions that are decorated on GO nanosheets. Such interactions would be highly facilitated when the 2D–2D interfacial arrangement is well maintained. In addition, CNs can hydrogen bond with GO nanosheets. Meanwhile, thermal decomposition of thiourea generated hydrogen sulfide which can react with interdigitated Sn^{4+} ions between GO nanosheets and CNs in order to form the layered structured of SnS_2 nanocrystals. As a result, the formation of 2D–2D interacting multilayered nanostructures is expected to successfully occur. In this work, ternary composites with varying amounts of CN but with the same amount of rGO and SnS_2 were synthesized. We modulated the relative amount of CN to rGO because the porous structure of the former would substantially minimize the volume change upon lithium ion insertion into the composites and the pores may act as extra spaces offering more active sites for lithium adsorption.[29,30] Moreover, CN can be considered a nitrogen-doped graphene with high nitrogen content. In general, heteroatom-doped graphene, especially with nitrogen, has shown increased capacity compared to pure graphene, although the origin of the enhanced capacity is not clearly shown.[31,32]

The phase and crystal structure of the synthesized ternary materials were characterized with powder X-ray diffraction (XRD). Fig. 1a shows X-ray diffractograms of SnS_2 and GSC6. All of the peaks in the diffraction pattern of SnS_2 can be indexed to

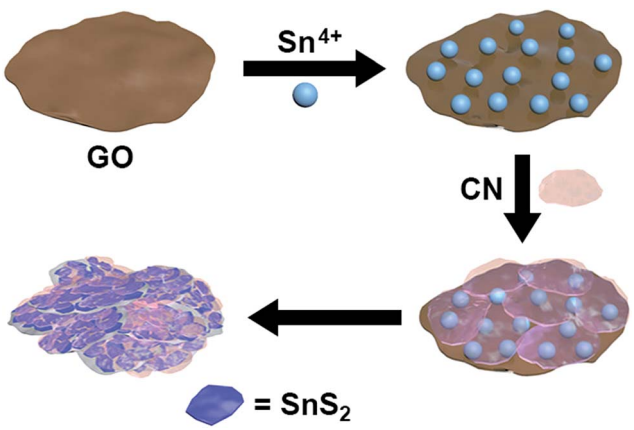

Scheme 1 Schematic of the synthesis of a 3D interdigitated and porous nano-architectured ternary composite of SnS_2, rGO and graphitic carbon nitride.

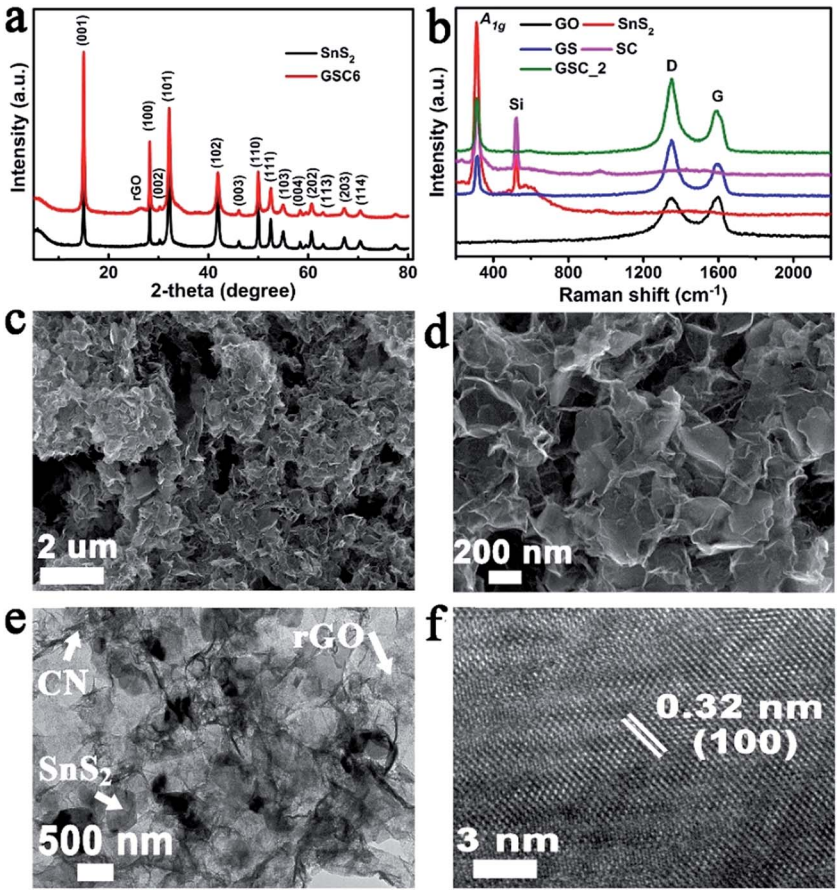

Fig. 1 (a) X-ray diffractograms of SnS_2 and GSC6. (b) Raman spectra of different samples. (c) and (d) SEM images of GSC6 with different magnifications. (e) and (f) TEM and high resolution TEM micrographs of GSC6, respectively.

the hexagonal SnS_2 (JCPDS card no. 23-0677).[5,33] No peaks from other phases were detected, indicating the presence of pure SnS_2. The diffractogram of GSC6 is similar to that of hexagonal SnS_2. However, the XRD pattern of GSC6 displays a low intensity peak at ~26°, which is due to the (002) planes of rGO.[34,35] This result and the absence of a peak at ~12° indicates the reduction of GO to rGO.[35,36] The chemical composition of the synthesized materials was further investigated by Raman spectroscopy, which is particularly sensitive and informative for characterizing carbon-based species. The Raman spectra of SnS_2 and SnS_2-based composites shown in Fig. 1b delineate a peak at 308.5 cm^{-1} that is assigned to the A_{1g} vibrational mode of SnS_2.[7] The peak at 523 cm^{-1} in the Raman spectra of SnS_2 and SC are due to the presence of the Si substrate.[37] However, this peak is absent in other samples, which is presumably due to the complete coverage of the Si substrate with the sample. Raman spectra of GO and the composites containing rGO show two peaks at 1351 cm^{-1} and 1486 cm^{-1} that are assigned respectively to the D and G bands of carbon materials.[7] The intensity ratio of the D band to G band (I_D/I_G) was increased from 0.99 in GO to 1.73 and 1.75 respectively in GS and GSC6. The increased values of the I_D/I_G ratio is ascribed to the formation of newly generated graphitic domain with smaller sizes compared to the original one in GO during the reduction process of GO to rGO and the presence of defects after partial reduction of GO.[7]

The morphological and structural characteristics of the ternary nanocomposites were investigated with field emission scanning electron microscopy (FESEM) and transmission electron microscopy (TEM). Fig. 1c and d depict FESEM micrographs of GSC6, in which 3D and porous structures of the nanocomposite are clearly manifested. Such a unique structure could facilitate faster electron transfer and lithium ion diffusion in the electrode. EDS and elemental mapping of GSC6 were delineated in Fig. S1,† which proved the presence of the elements Sn, S, C, O and N. Further information on the fine structure of the ternary nanocomposite was obtained from TEM observations. Fig. 1e illustrates the TEM image of GSC6, which clearly displays the presence of rGO (light gray background region), CN (darker regions with crumpled lines), and hexagonal SnS_2 plates, which stably remains in intimate contact with each other. This confirms the existence of 2D–2D type interfacial stacking among the component materials. In addition, a high resolution TEM (HRTEM) micrograph is portrayed in Fig. 1f, wherein the lattice fringe spacing of 0.32 nm clearly indicates the (100) planes of the hexagonal SnS_2.[6]

Detailed elemental composition and chemical states of the ternary nanocomposites were studied with X-ray photoemission spectroscopy (XPS). Survey XPS spectrum (Fig. 2a) of GSC6 shows main peaks at approximately 163, 284, 400, 487, and 531 eV that are due respectively to S, C, N, Sn, and O atoms. The

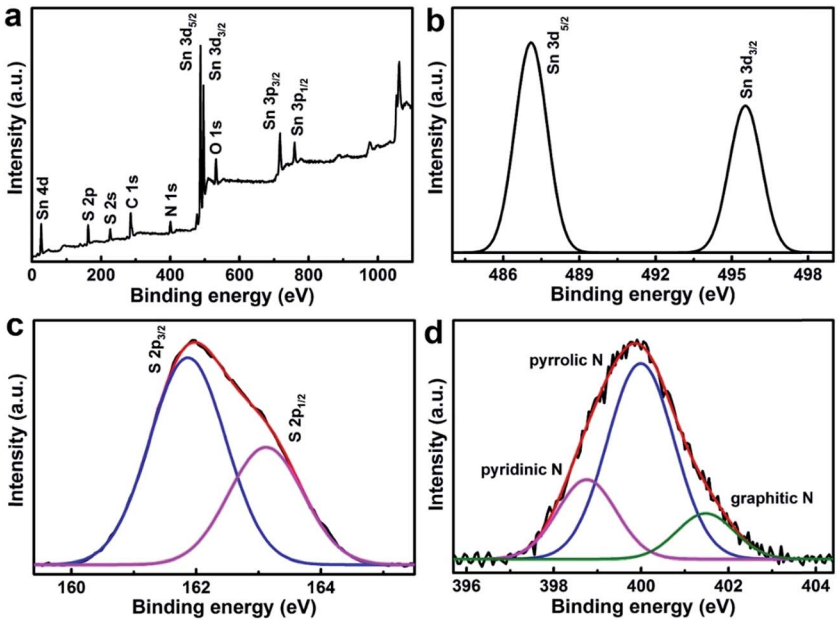

Fig. 2 X-ray photoemission spectra of GSC6: (a) survey spectrum; (b), (c), and (d) are high resolution spectra of Sn 3d, S 2p, and N 1s, respectively.

atomic ratio of S to Sn is calculated as 1.97, which is close to 2 (formation of SnS_2). Oxygen is present due to the inclusion of rGO and was 12.2 atom% compared to 29.7 atom% in GO. The valent state of Sn is further characterized with a high resolution XPS spectrum (Fig. 2b), which displays a doublet at 487.0 and 495.5 eV that are assigned respectively to Sn $3d_{5/2}$ and $3d_{3/2}$ of Sn^{4+} with a doublet spacing of ~8.5 eV, also indicative of the formation of SnS_2.[6,38] Fig. 2c portrays the core level XPS spectrum of S 2p in GSC6, which depicts a doublet at 161.8 and 163.1 eV for S $2p_{3/2}$ and S $2p_{1/2}$, respectively.[6,39] Similarly, Fig. S2† showed the bands at 161.2 and 162.3 eV respectively due to S $2p_{3/2}$ and S $2p_{1/2}$ of S^{2-}. Comparison of Fig. 2c and S2† clearly proved that the sulfur in GSC6 was due to S^{2-} of SnS_2 while excluding the possibility of S-doping in rGO, since the doped sulfur appears at higher energy in XPS spectra.[40,41] Additionally, XPS data reveals that GSC6 contains approximately 8.1 atom% nitrogen. Deconvolution of the N 1s peak (Fig. 2d) demonstrates that there are three types of nitrogen observed at 398.7, 400.0, and 401.4 eV, which designates the presence of pyridinic, pyrrolic, and graphitic N, respectively.[31] These peaks of N comprise 23.1, 64.0, and 12.9% of the total nitrogen content. Alternatively, GSC2 and GSC10 contain ~2.6 and ~11.3 atom% of nitrogen, respectively.

Next, thermogravimetric analysis (TGA) was employed to estimate the amount of carbon in GS and the subsequently calculated amount of CN in the ternary nanocomposites. Fig. 3a displays the TGA trace of GSC6, and those for GS, GSC2, and GSC10 are presented in Fig. S3.† All of the TGA traces undergo mainly two stages of weight loss due to the oxidative dissociation of rGO (or/and CN) and the oxidation of SnS_2 to SnO_2.[1] The carbon content in the nanocomposites is calculated on the basis of combined mass losses by the oxidation reactions of carbon and SnS_2.[42] The amount of carbon nitride in the ternary composites is then determined by subtracting the amount of carbon (in GS) from the total weight loss as all the composites (except SC) contain the same amount of GO. The amount of CN in GSC6 is determined to be 6.6 wt%. TGA data of GS, GSC2, and GSC10 are organized in Table S1.†

The microstructural features of the nano-architectures of ternary nanocomposites were confirmed from nitrogen adsorption–desorption isotherm measurements. The nitrogen sorption isotherm of GSC6 is depicted in Fig. 3b, which follows a typical type-IV pattern according to the IUPAC convention, indicating the existence of mesopores. The adsorption isotherm close to unity increases precipitously, characterizing the typical type II isotherm, which indicates the presence of macropores.[22] Alternatively, the sample shows a H3-type hysteresis loop, implying the presence of slit-like pores. The Brunauer–Emmett–Teller (BET) specific surface area of GSC6 is calculated to be 113 $m^2\ g^{-1}$. This high specific surface area of GSC6 may lead to a substantial increase in the electrode/electrolyte interfacial area, which could provide more sites for lithium insertion/desertion and superior electrochemical properties as an electrode. The inset in Fig. 3b delineates the pore size distribution, including pores of ~19.6 and ~60 nm in size, indicating the coexistence of mesopores and macropores as predicted from the N_2 sorption isotherms. The pore volume of GSC6 is determined to be 0.56 $cm^3\ g^{-1}$. The data obtained from the N_2 sorption curves for GSC6 are much greater than those from the SnS_2 hierarchical structure (68.1 $m^2\ g^{-1}$ and 21.1 nm) and the SnS_2/rGO composite (77.8 $m^2\ g^{-1}$, 5.37 nm and 0.10 $cm^3\ g^{-1}$) as compared to previously reported results. Such a high pore width and pore volume would efficiently alleviate the volume change of SnS_2 during cycling, which could eventually minimize the stress accumulation within the electrode. Nitrogen sorption data of CN, GSC2, and GSC10 are also structured in Table S2.†

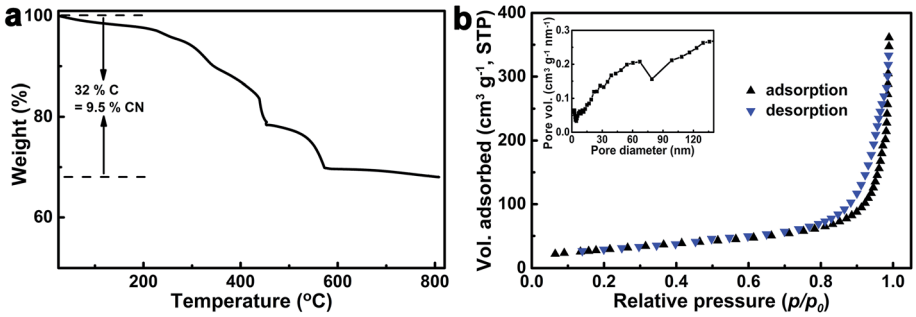

Fig. 3 (a) TGA result of GSC6. (b) Nitrogen sorption isotherm traces of GSC6.

Electrochemical properties

Electrochemical properties of the ternary composites were investigated with CR2032 type coin cells using lithium metal as the counter and reference electrodes, and the synthesized materials as the anode (working electrode). Fig. 4a depicts cyclic voltammograms (CVs) of the GSC6 nanocomposite within the potential window of 0.01 to 2.5 V at a scan rate of 0.1 mV s^{-1}. The first cathodic scan of GSC6 displays a peak at 1.86 V, which is not present in the successive scans, that can be attributed to lithium intercalation into the SnS_2 layers without causing phase decomposition, as shown in eqn (1).[5,11] The cathodic peaks at 1.60, 1.18, 1.02, and 0.89 V in the same scan correspond respectively to the lithium intercalation into the layers of SnS_2 (eqn (2)) and decomposition of SnS_2 to metallic Sn, which may occur in three consecutive steps, and the synchronous formation of Li_2S (eqn (3) and (4)) together with the formation of the solid electrolyte interface (SEI).[11,43] The SEI formation results in large irreversibility of the anode in the first charge–discharge cycle. The reduction peak at 0.05 V is due to the formation of Li_xSn alloys ($0 \leq x \leq 4.4$) (eqn (5)).[1,5]

The anodic peak in the first CV at 0.55 V is caused by the reversible de-alloying of the alloy Li_xSn into metallic Sn and Li (eqn (5)). The oxidation peak at 1.23 V and the prominent peak at 1.88 V may be attributed to the stepwise and reversible formation of SnS_2 by the reaction of Sn with Li_2S (eqn (6)) and oxygenation of metallic Sn and Li_2S, respectively.[44] The fourth oxidation peak appearing at 2.35 V, which does not exist in the successive cycles, might be due to the formation of S from Li_2S.[45] The second scan in the CV is associated with the alloying/de-alloying (0.10 V/0.58 V) together with lithium intercalation/de-intercalation (1.56 V/1.91 V) without phase decomposition, and the conversion reaction between SnS_2 and Li ions (1.03 V, 1.35 V/1.25 V). Notably, as evident from the 6th scan, CVs primarily exhibit two pairs of peaks at 1.56 V/1.92 V (Li intercalation/de-intercalation) and 1.34 V/1.41 V (eqn (6)) apart from alloying/de-alloying reactions.[42] It is worthy of mention that CVs nearly overlap with each other from the 8th scan, which implies the reversibility of the electrochemical processes and the formation of a stable SEI layer, both of which are imperative for obtaining high and stable reversible capacity. Moreover, in the 8th and subsequent scans, the redox peaks at 1.34 and 1.41 V are consistently present, also implying the partial reversibility of eqn (6).[44] The CVs of SnS_2 are shown in Fig. S4,† which closely resemble the CVs of GSC in the first scan. Notably, CVs of SnS_2 do not show peaks at 1.34 V and 1.41 V after the first scan, indicating serious irreversibility and leading to capacity fading of the electrode.[44] The maximum theoretical capacity of SnS_2 is calculated to be 1232.2 mA h g^{-1} based on the reversibility of eqn (4) and (5).[3,11] The electrochemical reactions of SnS_2 with lithium ions during charge–discharge processes are outlined as follows:

$$SnS_2 + xLi^+ + xe^- \rightarrow Li_xSnS_2 \quad (1)$$

$$Li_xSnS_2 + (y - x)Li^+ + (y - x)e^- \rightarrow Li_ySnS_2 \quad (2)$$

$$Li_ySnS_2 + (4 - y)Li^+ + (4 - y)e^- \rightarrow Sn + Li_2S\ (0 < x < y \leq 2) \quad (3)$$

$$SnS_2 + 4Li^+ + 4e^- \rightarrow Sn + 2Li_2S \quad (4)$$

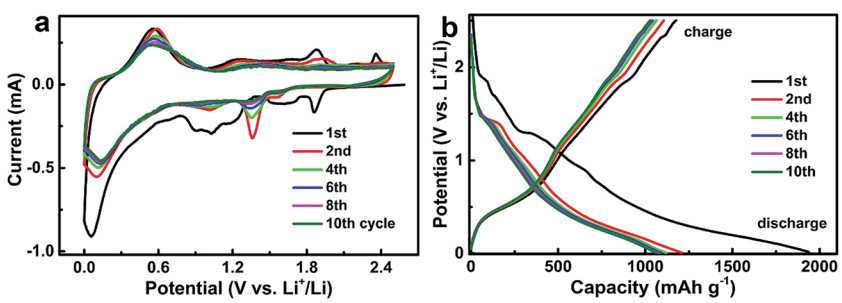

Fig. 4 (a) CV profiles of GSC6 and (b) voltage profiles of GSC6.

$$Sn + 4.4Li^+ + 4.4e^- \leftrightarrow Li_{4.4}Sn \quad (5)$$

$$Sn + 2Li_2S \leftrightarrow SnS_2 + 4Li^+ + 4e^- \quad (6)$$

Fig. 4b unveils the selected voltage profile of GSC6 at a current density of 100 mA g^{-1} in the potential range between 0.005 and 2.5 V. In the first discharge cycle, a plateau appears at 1.9 V, which is due to the intercalation of lithium ions into the layered SnS_2 without phase decomposition, whereas the plateaus observed at 1.7, 1.3, and 0.9 V are due to the decomposition of SnS_2 to Sn and Li_2S and the formation of SEI.[46] Alternatively, the first charge curve shows plateaus at 0.4 V (de-alloying reaction), 1.1, and 1.8 V that are attributed to the formation of SnS_2 and de-intercalation of Li ions from SnS_2. Moreover, the interpretation of the plateau at 2.3 V is identical to that in CV and successive curves follow the same discussion. The charge–discharge profiles clearly show that discharge curves (and charge curves also) overlap with each other after the 8th cycle, which indicates full reversibility of the electrode reactions. Obviously, the obtained data for CV curves and voltage profiles are consistent with each other. The first discharge and charge capacities are 1939 and 1186 mA h g^{-1}, respectively. Such a high irreversibility is attributed to the incomplete conversion reaction, the formation of SEI related to the irreversible loss of lithium ions, and the reaction of lithium ions with oxygen containing functional groups in rGO.

It should be noted here that the first discharge capacity is much greater than the maximum theoretical capacity of SnS_2 (1232.2 mA h g^{-1}), which is possibly ascribed to the following reasons.[45] In general, due to the large surface-to-volume ratio in nanoarchitectures compared to their bulk counterparts, these materials may have high surface energy that can accelerate many side reactions between the electrode and electrolyte, leading to irreversible trapping of a large quantity of lithium ions.[11,47] The formation and decomposition of Li_2S (appearing at 2.35 and 1.88 V respectively in the first anodic CV trace, which is not present in the successive scans) also consume lithium ions during the first cycle, which induces a high discharge capacity.[5] Moreover, the reaction of lithium ions with oxygen containing functional groups in the composite is also responsible for the high discharge capacity (than theoretical value). Excessively large initial discharge capacity resulting in large amount of trapped irreversibly trapped lithium ions, eventually leading to low Coulombic Efficiency (CE) in the first cycle. The CE of GSC6 was increased from 61.1% to 91.3% in the second cycle, and eventually reached >99% after the 18th cycle. The initial CEs of all the controls are displayed in Table S3.†

Fig. 5a represents the galvanostatic charge–discharge performance of GSC6 and the reference samples at 100 mA g^{-1}. Pristine SnS_2 shows a discharge capacity of 235.8 mA h g^{-1} and a CE of 98.2% after 100 cycles due to the severe capacity fading. On the other hand, g-C_3N_4 only exhibits a capacity of 18.5 mA h g^{-1} after sixty cycles with CE 98.5%. The composite SC displayed a discharge capacity of 240.1 mA h g^{-1} and a CE of 98.6% after 100 cycles. Alternatively, the anode performance of SnS_2 is greatly improved in GS, which exhibits a discharge capacity of 614.9 mA h g^{-1} and a CE of 98.9% after the same number of cycles. Such an improvement in the specific capacity might be explained by high conductivity and a volumetric relaxation effect provided by the rGO nanosheets.

Additionally, a more significantly improved cycle performance is observed for GSC6, with a discharge capacity of 1248.4 mA h g^{-1} and a CE of 99.9% after 276 cycles. This excellent charge–discharge performance is possibly attributed to the maximized cushioning effect offered by both rGO and CN along with the highly porous structure of the nanocomposites, which

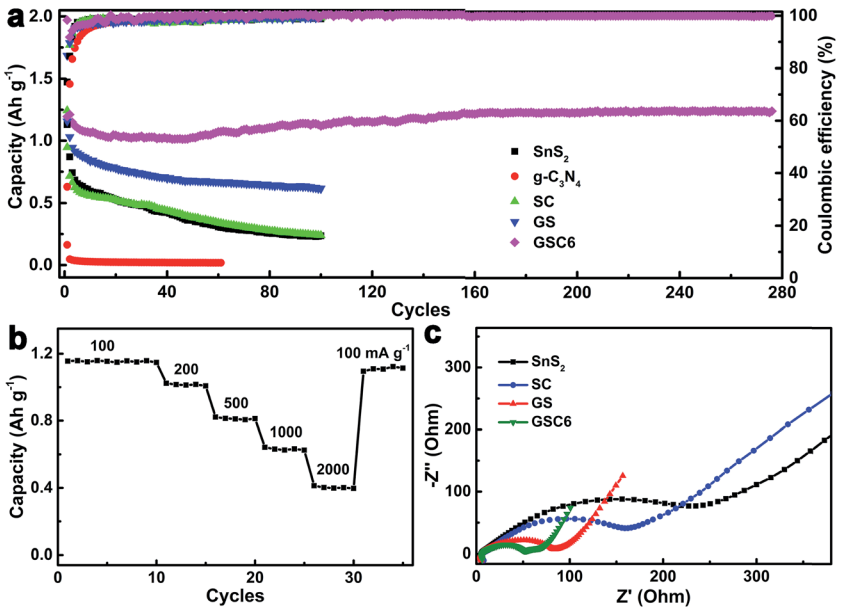

Fig. 5 (a) Cyclic stability of GSC6 and different controls, (b) rate performance of GSC6, and (c) electrochemical impedance spectra of different samples.

can efficiently accommodate the volume change of SnS_2 and increase the conductivity of the composite. In addition, rate capability tests for GSC6 were performed to understand its stability under different discharge current densities. Fig. 5b shows that GSC6 demonstrates a discharge capacity of 1108 mA h g^{-1} at a 100 mA g^{-1} discharge rate. At 2000 mA g^{-1} of discharge current density, the specific capacity decreased to 396 mA h g^{-1} which is higher than the theoretical capacity of graphite (372 mA h g^{-1}). When the discharge current density returns to 100 mA g^{-1}, the specific capacity returns to 1102 mA h g^{-1} and this value is retained in the subsequent cycles. Therefore, the rate performance studies undoubtedly prove the outstanding stability of GSC6 under varied current density conditions and its strong potential as an excellent candidate for high performance anode materials.

In order to elucidate the outstanding cyclic stability and excellent rate performance of the GSC6 ternary nanocomposite, the electrochemical impedance spectroscopy (EIS) was employed and the results were compared to the control samples. The EIS curves depicted in Fig. 5c delineates a straight slope line in the low frequency region and a depressed semi-circular arc in the mid to high frequency region for each material. The inclined straight line in the low frequency region indicates Warburg impedance related to the diffusion of lithium ions into the bulk of the electrode. Meanwhile, the semi-circular arc at the mid/high frequency describes the charge-transfer resistance at the electrode–electrolyte interface. It is evident from Fig. 5c that pristine SnS_2 has the highest charge-transfer resistance because of its low conductivity. The charge-transfer resistance is decreased in the binary composites of SC and GS due to the presence of CN and rGO, respectively, although the effect is more pronounced in GS as the rGO is much more electroconductive than CN. As expected, the GSC6 nanocomposite shows the smallest semi-circle, thereby indicating the lowest charge-transfer resistance and interfacial resistance, *i.e.*, the fastest charge-transfer reaction for the lithium ion insertion and desertion assisted by high electrical conductivity.

Apart from the comparison of the charge-transfer resistance, the relative rate of the lithium ion diffusion is assessed to demonstrate the excellent electrochemical properties of GSC6, for which the real part of the impedance Z' is plotted against $\omega^{-0.5}$ in rad s^{-1} (where the angular frequency ω is equal to $2\pi f$ and f is the linear frequency in Hz) as depicted in Fig. 6a.[48,49] The slope of each curve is calculated and arranged in the inset table, which shows that the slope of SnS_2, SC, GS, and GSC6 are determined respectively to be 360.5, 257.0, 27.9, and 20.8. GSC6 has the lowest slope as a result of the highest lithium ion diffusion coefficient among all of the composites. Overall, the lowest charge-transfer resistance and the highest lithium ion diffusion rate can synergistically result in the best electrochemical performances in GSC6.

Moreover, the EIS of the GSC6 electrode after cycling was measured and compared to the pristine electrode, as depicted in Fig. 6b. Both of the impedance spectra show a low frequency line (Warburg impedance) and semi-circle at mid and high frequency region. Comparison of the two impedance spectra clearly shows that the radius of the semi-circular arc of the electrode after cycling is smaller than before cycling. This result evidently demonstrates that the charge-transfer resistance of the electrode after cycling decreases compared to that before cycling, thereby indicating highly enhanced electronic and ionic conductivities of the electrode during cycling.[50] Consequently, this electrode could show excellent cyclic stability and rate performances. The electrode made of GSC6 was then disassembled and analyzed for morphological studies by FESEM, as depicted in Fig. 6d. For a comparison, the FESEM micrograph of pristine electrode is also displayed in Fig. 6c. Comparative observations show that the structural integrity of the electrode is strongly retained even after multiple discharging operations at high current density (2 A g^{-1}). Once again, this

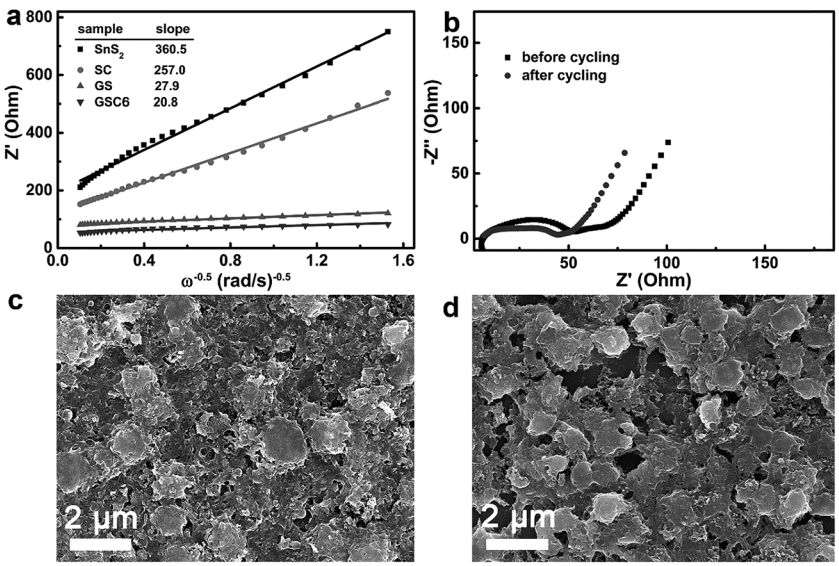

Fig. 6 (a) Plot of Z' *vs.* $\omega^{-0.5}$ of different samples. (b) Impedance spectra of the GSC6 electrode before and after the cycle. SEM micrographs of the GSC6 electrodes (c) before and (d) after the cycling test.

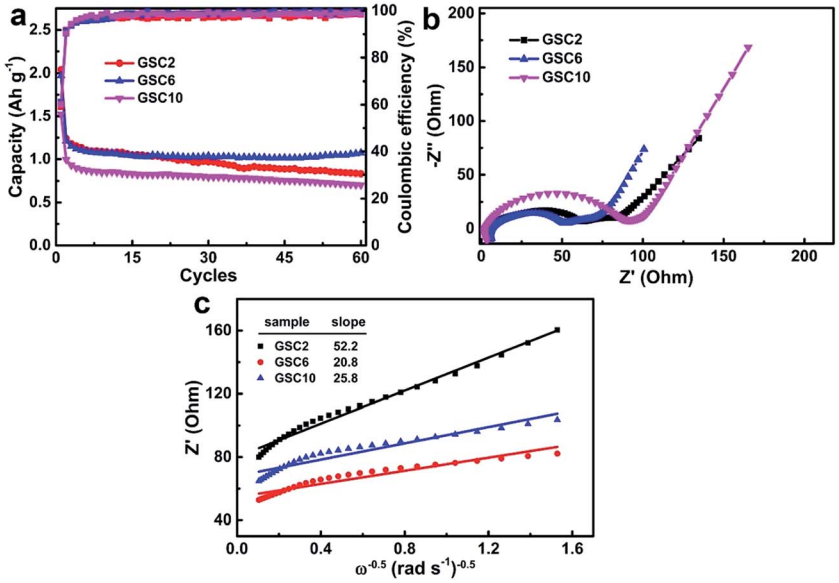

Fig. 7 Comparison of anode performances with different amount of CNs. (a), (b), and (c) Cyclic stability, impedance spectra, and Z' *vs.* $\omega^{-0.5}$ plot of all the ternary composites, respectively.

result clearly demonstrates the excellent stability of the GSC6 electrode.

For a more profound understanding on the effect of the inclusion of CN on the increased specific capacity, three different ternary composites were compared in their electrochemical performances (GSC2, GSC6, and GSC10). Initial CE of GSC2 and GSC10 were displayed in Table S3.† Galvanostatic charge–discharge curves for GSC2 and GSC10 at 100 mA g^{-1} are depicted in Fig. 7a. For a comparison, the charge–discharge curve of GSC6 is also displayed in this figure. Fig. 7a shows that the cyclic performance of the composites increases with increasing CN from 2.0 wt% to 6.6 wt%, but it then decreases when the loading further increases to 10.5 wt%. Additionally, the ternary composites of GSC2, GSC6, and GSC10 display discharge capacities of 830.9, 1073.1, and 702.7 mA h g^{-1} and the corresponding CEs of 98.5, 99.6, and 98.6%, respectively, after sixty cycles. To explain this difference, the EIS of the nanocomposites are measured and portrayed in Fig. 7b, which illustrates that the charge-transfer resistance and interfacial resistance first decreases from GSC2 to GSC6 and then increases in GSC10. Moreover, plots of Z' *vs.* $\omega^{-0.5}$, depicted in Fig. 7c, show slope values of 52.2, 20.8, and 25.8, respectively, for GSC2, GSC6, and GSC10. Therefore, these plots and data well explain that GSC6 has the highest Li ion diffusion coefficient among all the ternary composites. As a result, GSC6 could possess the highest electrical conductivity, the fastest charge-transfer reaction, and the highest lithium ion diffusion rate, which are amenable for the best electrochemical performances. Table S3† also summarizes the cyclic performance and CE of all of the synthesized materials. Moreover, the performance of the GSC6 electrode is compared to recently reported state-of-the-art SnS_2-based anodes and the values are organized in Table S4,† revealing the best performances of the present anodes among those reported.

On the basis of the above-mentioned experimental results and discussion, the extraordinary electrochemical properties of GSC6 are ascribed to the following reasons. First, a unique 3D porous nano-architecture is created by face-to-face interactions between SnS_2, CN, and rGO, ensuring a high interfacial contact area, faster electron transport, and accelerated lithium ion diffusion for the improved reaction kinetics. Second, porous structures of the ternary nanocomposite alleviate the volume change of SnS_2 during cycling, which enables retention of the structural integrity of the electrode, even after discharging at high current densities, without sacrificing the impedance characteristics of the electrode. Moreover, pores in the nano-architecture allow for efficient transport of lithium ions and electrolyte, offering good accessibility of ions and electrolytes to the SnS_2 (active electrode material) particles. Third, a high specific surface area of the 3D nano-architectures ensures the extended electrode/electrolyte interfacial area and correspondingly increased lithium ion diffusivity across the electrode–electrolyte interfaces. Additionally, a high surface area creates more sites for lithium ion insertion/extraction during cycling, also contributing to the improved electrochemical performances. Lastly, a decrease in the charge-transfer resistance leads to faster charge-transfer kinetics and a higher lithium ion diffusion coefficient, enabling the electrode to exhibit remarkable electrochemical performances to attain the theoretical capacity of SnS_2.

Conclusions

In summary, 3D porous nano-architectures were synthesized by combining three 2D materials of SnS_2, rGO, and g-C_3N_4 through a one-pot hydrothermal treatment. The obtained nanocomposites have shown high BET specific surface area and porous structures. Tests for the lithium ion battery anode

revealed that the performances of the ternary nanocomposites were superior to those of the nanocomposites of rGO–SnS_2. Moreover, galvanostatic charge–discharge experiments illustrated that the cyclic stability of ternary nanocomposites is strongly affected by the amount of incorporated g-C_3N_4. The composite containing ~10.7 wt% of rGO and ~6.6 wt% of g-C_3N_4 exhibited the best performance with a specific capacity of 1248.4 mA h g^{-1} and a coulombic efficiency of 99.9% after 276 cycles at a discharge rate of 100 mA g^{-1}. Apart from this result, the composites also showed excellent rate performance. Outstanding performances of the highly interdigitated ternary nanocomposites could be attributed to the highly increased contact area *via* face-to-face arrangements between tertiary constituents and a highly porous structure, which alleviates the volume change of SnS_2 during cycling. As a result, the electrodes have undergone minimum strain and their structural integrity was well retained. Moreover, low charge-transfer resistance and a high lithium ion diffusion coefficient have confirmed faster electronic and ionic transport within the electrodes. Therefore, it is anticipated that such 3D porous nano-structuring harnessing the 2D–2D interactions between planar nanomaterials could be expanded to other metal sulfides and oxides for application to ultrahigh energy storage and superfast charging/discharging capabilities in Li-ion battery anodes.

Acknowledgements

This work was supported by research grants of the NRF (2014M3A7B4052200, 2014M3C1A3053035) and Basic Science Research Program (2010-0027955) funded by the National Research Foundation under the Ministry of Science, ICT & Future, Korea.

References

1 L. Mei, C. Xu, T. Yang, J. Ma, L. Chen, Q. Li and T. Wang, *J. Mater. Chem. A*, 2013, **1**, 8658–8664.
2 J. W. Seo, J. T. Jang, S. W. Park, C. Kim, B. Park and J. Cheon, *Adv. Mater.*, 2008, **20**, 4269–4273.
3 J. Zai, K. Wang, Y. Su, X. Qian and J. Chen, *J. Power Sources*, 2011, **196**, 3650–3654.
4 Q. Zhang, R. Li, M. Zhang, B. Zhang and X. Gou, *Electrochim. Acta*, 2014, **115**, 425–433.
5 L. Ji, H. L. Xin, T. R. Kuykendall, S.-L. Wu, H. Zheng, M. Rao, E. J. Cairns, V. Battaglia and Y. Zhang, *Phys. Chem. Chem. Phys.*, 2012, **14**, 6981–6986.
6 W. Sun, X. Rui, D. Yang, Z. Sun, B. Li, W. Zhang, Y. Zong, S. Madhavi, S. Dou and Q. Yan, *ACS Nano*, 2015, **9**, 11371–11381.
7 B. Luo, Y. Fang, B. Wang, J. Zhou, H. Song and L. Zhi, *Energy Environ. Sci.*, 2012, **5**, 5226–5230.
8 X. An, J. C. Yu and J. Tang, *J. Mater. Chem. A*, 2014, **2**, 1000–1005.
9 S. Y. Hong, R. Popovitz-Biro, Y. Prior and R. Tenne, *J. Am. Chem. Soc.*, 2003, **125**, 10470–10474.
10 Y. Liu, H. Kang, L. Jiao, C. Chen, K. Cao, Y. Wang and H. Yuan, *Nanoscale*, 2015, **7**, 1325–1332.
11 L. Wang, L. Zhuo, Y. Yu and F. Zhao, *Electrochim. Acta*, 2013, **112**, 439–447.
12 X. Zhang, Y. Zhan, F. Xie, W. Zhang, J. Chen, W. Xie, W. Mai and H. Meng, *Electrochemistry*, 2016, **84**, 420–426.
13 D. Li and G. S. Sur, *Macromol. Res.*, 2014, **22**, 113–116.
14 Y. A. Attia, *Mater. Express*, 2016, **6**, 211–219.
15 Y. Lee and J.-H. H. Ahn, *Nano*, 2013, **8**, 1330001.
16 K. Chang, Z. Wang, G. Huang, H. Li, W. Chen and J. Y. Lee, *J. Power Sources*, 2012, **201**, 259–266.
17 C. Gao, L. Li, A. R. O. Raji, A. Kovalchuk, Z. Peng, H. Fei, Y. He, N. D. Kim, Q. Zhong, E. Xie and J. M. Tour, *ACS Appl. Mater. Interfaces*, 2015, **7**, 26549–26556.
18 X. Wang, K. Maeda, A. Thomas, K. Takanabe, G. Xin, J. M. Carlsson, K. Domen and M. Antonietti, *Nat. Mater.*, 2009, **8**, 76–80.
19 J. Zhu, P. Xiao, H. Li and A. C. Carabineiro, *ACS Appl. Mater. Interfaces*, 2014, **6**, 16449–16465.
20 W. J. Ong, L. L. Tan, Y. H. Ng, S. T. Yong and S. P. Chai, *Chem. Rev.*, 2016, **116**, 7159–7329.
21 G. Dong, Y. Zhang, Q. Pan and J. Qiu, *J. Photochem. Photobiol., C*, 2014, **20**, 33–50.
22 A. Cheng, H. Huan, T. C. Sum, R. Ahuja and Z. Chen, *ACS Appl. Mater. Interfaces*, 2013, **5**, 10317–10324.
23 Y. Hou, J. Li, Z. Wen, S. Cui, C. Yuan and J. Chen, *Nano Energy*, 2014, **8**, 157–164.
24 Z. Zhang, J. Huang, M. Zhang, Q. Yuan and B. Dong, *Appl. Catal., B*, 2015, **163**, 298–305.
25 M. S. A. Sher Shah, W. J. Kim, J. Park, D. K. Rhee, I. H. Jang, N. G. Park, J. Y. Lee and P. J. Yoo, *ACS Appl. Mater. Interfaces*, 2014, **6**, 20819–20827.
26 M. S. A. Sher Shah, K. Zhang, A. R. Park, K. S. Kim, N.-G. Park, J. H. Park and P. J. Yoo, *Nanoscale*, 2013, **5**, 5093–5101.
27 M. S. A. Sher Shah, S. Muhammad, J. H. Park, W.-S. Yoon and P. J. Yoo, *RSC Adv.*, 2015, **5**, 13964–13971.
28 X. Fan, L. Zhang, R. Cheng, M. Wang, M. Li, Y. Zhou and J. Shi, *ACS Catal.*, 2015, **5**, 5008–5015.
29 M. Hankel, D. Ye, L. Wang and D. J. Searles, *J. Phys. Chem. C*, 2015, **119**, 21921–21927.
30 T. S. Miller, A. B. Jorge, A. Sella, F. Corà, P. R. Shearing, D. J. L. Brett and P. F. McMillan, *Electroanalysis*, 2015, **27**, 2614–2619.
31 F. Zheng, Y. Yang and Q. Chen, *Nat. Commun.*, 2014, **5**, 5261.
32 L.-L. Tian, X.-Y. Wei, Q.-C. Zhuang, C.-H. Jiang, C. Wu, G.-Y. Ma, X. Zhao, Z.-M. Zong and S.-G. Sun, *Nanoscale*, 2014, **6**, 6075–6083.
33 C. Zhai, N. Du and H. Z. D. Yang, *Chem. Commun.*, 2011, **47**, 1270–1272.
34 J. Xiao, X. Wang, X. Q. Yang, S. Xun, G. Liu, P. K. Koech, J. Liu and J. P. Lemmon, *Adv. Funct. Mater.*, 2011, **21**, 2840–2846.
35 Y. Zou and Y. Wang, *Nanoscale*, 2011, **3**, 2615–2620.
36 J. S. Chen, Z. Wang, X. C. Dong, P. Chen and X. W. D. Lou, *Nanoscale*, 2011, **3**, 2158–2161.
37 M. Khorasaninejad, J. Walia and S. S. Saini, *Nanotechnology*, 2012, **23**, 275706.
38 M. Sathish, S. Mitani, T. Tomai and I. Honma, *J. Phys. Chem. C*, 2012, **116**, 12475–12481.

39 T. Wang, H. Meng, X. Yu, Y. Liu, H. Chen, Y. Zhu, J. Tang, Y. Tong and Y. Zhang, *RSC Adv.*, 2015, **5**, 15469–15478.
40 G. Zhou, E. Paek, G. S. Hwang and A. Manthiram, *Nat. Commun.*, 2015, **6**, 7760.
41 B. Quan, S. H. Yu, D. Y. Chung, A. Jin, J. H. Park, Y. E. Sung and Y. Piao, *Sci. Rep.*, 2014, **4**, 5639.
42 G. Wang, J. Peng, L. Zhang, J. Zhang, B. Dai, M. Zhu, L. Xia and F. Yu, *J. Mater. Chem. A*, 2015, **3**, 3659–3666.
43 T. J. Kim, C. Kim, D. Son, M. Choi and B. Park, *J. Power Sources*, 2007, **167**, 529–535.
44 Y. Jiang, Y. Feng, B. Xi, S. Kai, K. Mi, J. Feng, J. Zhang and S. Xiong, *J. Mater. Chem. A*, 2016, **4**, 10719–10726.
45 S. Yan, K. Li, Z. Lin, H. Song, T. Jiang, J. Wu and Y. Shi, *RSC Adv.*, 2016, **6**, 32414–32421.
46 D. Guan, J. Li, X. Gao and C. Yuan, *RSC Adv.*, 2015, **5**, 58514–58521.
47 P. G. G. Bruce, B. Scrosati and J.-M. Tarascon, *Angew. Chem., Int. Ed. Engl.*, 2008, **47**, 2930–2946.
48 Y. J. Hong, M. Y. Son and Y. C. Kang, *Nano Lett.*, 2013, **13**, 5462–5466.
49 Y. Shi, J. Wang, S. Chou, D. Wexler, H. Li, K. Ozawa, H. Liu and Y. Wu, *Nano Lett.*, 2013, **13**, 4715–4720.
50 Y. Sun, J. Wang, B. Zhao, R. Cai, R. Ran and Z. Shao, *J. Mater. Chem. A*, 2013, **1**, 4736–4746.